

FAST HI 21 cm study of blueberry galaxies

YOGESH CHANDOLA,¹ CHAO-WEI TSAI,^{2,3,4} D.J. SAIKIA,⁵ GUODONG LI,^{6,2} DI LI,^{7,2} AND YIN-ZHE MA⁸

¹*Purple Mountain Observatory, Chinese Academy of Sciences, 10 Yuan Hua Road, Qixia District, Nanjing 210023, People's Republic of China*

²*National Astronomical Observatories, Chinese Academy of Sciences, 20A Datun Road, Beijing 100101, People's Republic of China*

³*Institute for Frontiers in Astronomy and Astrophysics, Beijing Normal University, Beijing 102206, People's Republic of China*

⁴*School of Astronomy and Space Science, University of Chinese Academy of Sciences, Beijing 100049, People's Republic of China*

⁵*Inter-University Centre for Astronomy and Astrophysics (IUCAA), Pune 411007, India*

⁶*Kavli Institute for Astronomy and Astrophysics (KIAA), Peking University, Beijing 100871, People's Republic of China*

⁷*Department of Astronomy, Tsinghua University, Beijing 100084, People's Republic of China*

⁸*Department of Physics, Stellenbosch University, Matieland 7602, South Africa*

ABSTRACT

Green Peas (GPs) and blueberry galaxies (BBs) are thought to be local analogs ($z < 0.1$) of high redshift Ly α emitters. HI study of these can help us understand the star formation in the primordial Universe. In this Letter, we present the results of HI 21 cm study of 28 high specific star formation rate (sSFR $\gtrsim 10^{-8}$ yr $^{-1}$) BBs at $z \lesssim 0.05$ with the Five-hundred-meter Aperture Spherical radio Telescope. We report significant HI detection towards two BBs namely J1026+0426 and J1132+0809, and discuss possible HI contribution from neighboring galaxies. The median 3σ upper limit of $\sim 2.0 \times 10^8 M_{\odot}$ was obtained on HI mass for galaxies with nondetections. We find BBs tend to have lower HI-to-stellar mass ratio or gas fraction (f_{HI}) than expected from f_{HI} -sSFR and f_{HI} - M_{\star} relations for main-sequence galaxies. The BBs also have a median 3σ upper limit on HI gas depletion time scale (τ_{HI}) ~ 0.5 Gyr, about 1 order of magnitude lower than τ_{HI} for local main-sequence galaxies. We find a significantly low HI detection rate of 2/28 ($7.1_{-4.6}^{+9.4}$ %) towards these galaxies, which is similar to previous HI studies of low redshift GPs of high ionization parameter indicator, O32 \equiv O[III] λ 5007/O[II] λ 3727 ratios $\gtrsim 10$.

Keywords: Galaxies (573); H I emission (690); Radio spectroscopy(1359); Starburst galaxies(1570); Blue compact dwarf galaxies(165)

1. INTRODUCTION

To understand star-formation near reionization in the early primordial Universe, there have been many searches for high redshift galaxies, such as the Ly α emitters (LAE; Gawiser et al. 2007). LAEs are compact, low stellar mass galaxies with very low metallicity and strong Ly α emission in the high redshift ($z > 2$) Universe. However, because of the instrumental limitations, it is difficult to study high redshift objects comprehensively. Hence, the properties of local LAE analogs such as Green Peas (GPs; Cardamone et al. 2009) provide crucial hints about the physical processes in these

compact and low metallicity systems. GPs like LAEs are compact, low metallicity systems at relatively lower redshifts ($z \lesssim 0.3$). Studies by Izotov et al. (2016, 2018a,b) find Lyman continuum (LyC) leakage in significant amounts (2%-72%) in some GP galaxies sufficient to ionize the neutral hydrogen in the intergalactic medium. Recently, Yang et al. (2017a) discovered a similar class of galaxies termed ‘blueberry’ galaxies (BBs) in the nearby Universe ($z \lesssim 0.05$). These galaxies are very compact ($\lesssim 1$ kpc in linear projected size) and have small a star formation rate (SFR), but these are high specific star formation rate (sSFR $> 10^{-8}$ yr $^{-1}$) starburst systems. These systems are characterized by their extreme emission line ratios (O[III] λ 5007/O[II] λ 3727 ~ 8 -60) and extreme blue colors ($g-r < -0.5$ mag and $r-i < 1$ mag). Most of these have very low stellar mass ($M_{\star} \sim 10^{6.5-8.5} M_{\odot}$) and some of these systems also have

very low metallicities ($Z \lesssim 1/10 Z_{\odot}$) which make them similar to higher redshift ($z > 0.1$) GPs and LAEs. GPs owe their green color to the strong $\text{O}[\text{III}]\lambda 5007$ emission line with large equivalent widths ($\sim 1000 \text{ \AA}$) falling in the Sloan Digital Sky Survey (SDSS; Abazajian et al. 2009) ‘*r*’ band while for lower redshift BBs it falls in the ‘*g*’ band making their color appear blue. Compared to several other star-forming dwarf galaxies like local blue compact dwarfs (BCDs; Gil de Paz et al. 2003), these systems have similar stellar mass, but higher emission line strength and gas ionization, and hence reside at extreme top-left in the Baldwin-Phillips-Terlevich (BPT; Baldwin et al. 1981) diagram.

HI 21cm line can be used to trace the cold gas fuel reservoir for these systems. Though there have been earlier HI studies on the starburst BCDs, most of them have sSFRs $< 10^{-8} \text{ yr}^{-1}$ (Chandola et al. 2024). In our recent work, we studied HI gas contents toward 11 mid-infrared (IR) bright BCDs of sSFR $\sim 10^{-8} \text{ yr}^{-1}$ with the Arecibo telescope, where we have detections toward six sources (Chandola et al. 2024). Mid-IR bright BCDs observed with the Arecibo telescope were found to have a very low HI gas depletion time scale of ~ 0.3 Gyr (Chandola et al. 2024). It indicates that these systems will deplete their gas reservoir quite fast due to their high SFR. Previously, from a sample of 40 GPs at low redshift $z < 0.1$ selected from Jiang et al. (2019), Kanekar et al. (2021) found that GPs have a very low depletion time scale of ~ 0.6 Gyr and sources with higher $\text{O}[\text{III}]\lambda 5007/\text{O}[\text{II}]\lambda 3727$ have low HI detection rates. Like BCDs in our Arecibo study (Chandola et al. 2024) and GPs from Kanekar et al. (2021), BBs are very high sSFR systems but have lower SFR and slightly lower stellar mass. Hence, to get a complete picture, it is important to probe whether these systems have similar low depletion time scales for different ranges of stellar masses and SFRs. BBs also have very high $\text{O}[\text{III}]\lambda 5007/\text{O}[\text{II}]\lambda 3727$ (O32) ratios and hence form a useful sample to test the presence of an atomic HI reservoir in extreme conditions. Recently, Dutta et al. (2024) studied HI content toward one of the BBs, J1509+3731, to find a very low depletion time scale of ~ 0.2 Gyr indicating fast depletion of HI reservoir. Interferometric HI studies of BBs and nearby GPs suggest a merger origin (Purkayastha et al. 2022; Dutta et al. 2024).

In this Letter, we present the HI observation results of a sample of 28 BBs from Yang et al. (2017a) with the Five-hundred-meter Aperture Spherical radio Telescope (FAST; Nan et al. 2011) obtained during 2020-2023 (see Table. 1). This is the largest sample of BBs with high O32 ratios studied in HI. We describe the observations and data reduction process in Section 2. We present

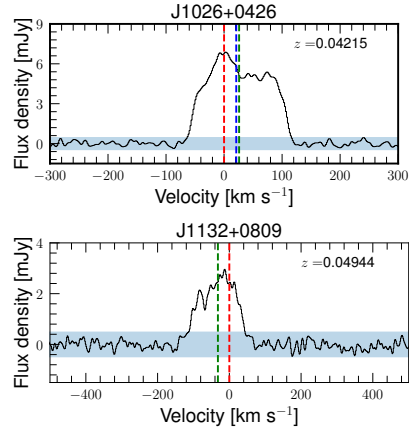


Figure 1. 21 cm emission spectra of blueberry galaxies with HI detections. The X-axes show the velocity relative to optical systemic velocity (cz) at the heliocentric frame in km s^{-1} . The Y-axes show the flux density in mJy. Blue shades mark the 3σ noise levels. Red vertical dashed lines mark the zero relative velocity corresponding to the optical redshift of the blueberry galaxies. Green vertical dashed lines mark the HI velocity (V_{HI}) relative to the optical systemic velocity. In the upper panel, the blue dashed vertical line marks the optical systemic velocity of the neighboring spiral galaxy relative to the optical velocity of blueberry galaxy J1026+0426.

and discuss results in Section 3. We summarize them in Section 4. We use the concordance cosmology $H_0 = 70 \text{ km s}^{-1} \text{ Mpc}^{-1}$, $\Omega_m = 0.3$, $\Omega_\Lambda = 0.7$.

2. OBSERVATIONS AND DATA REDUCTION

The observations toward the BBs were executed in two phases. In the first phase from 2020 September to 2021 February, observations were carried out toward 21 sources for 15.1 hr (including overheads) using the standard ON and OFF position mode of FAST (project code: PT2020_0082). In this phase, the OFF position was made by shifting $18'$ in the R.A. toward the west. However, the observations of 20 sources were severely affected due to the radio frequency interference (RFI) from the feed compressor. In the second phase 2022 August-2023 May, the observations were done for 27 sources for 19.2 hr (project code: PT2022_0192), including those 20 sources that were affected by RFI in the first phase of observations. In the second phase of observations, the OFF position was made by shifting $11.8'$ toward the west, so that we have another beam, M08, at the ON position of the target source while the central beam is at the OFF position. We used a sampling time of 1 s and injected low (1 K) noise for 1 s after every 2 s in all the observations for calibration. The observational details along with source properties are provided in Table 1. The total observing ON source time varies from 3 minutes to 96 minutes.

Table 1. Characteristics of observed BBs

(1)	(2)	(3)	(4)	(5)	(6)	(7)	(8)	(9)	(10)	(11)	(12)
Source Name (ID)	D_L (Mpc)	Date of Ob.	Beam(s) Used	Time (s)	ΔS_{rms} (mJy)	$\log M_{HI}$ (M_\odot)	$\log M_*$ (M_\odot)	$\log \text{SFR}$ ($M_\odot \text{ yr}^{-1}$)	$\log f_{HI}$	$\log \tau_{HI}$ (yr)	$\log \text{O32}$
J0146+0319 (27)	207.1	2022 Aug 22	M01,M08	360	0.32	<8.34	7.7	0.06	<0.64	<8.27	1.07
J0216+1715 (28)	173.0	2022 Aug 22	M01,M08	1980	0.15	<7.85	6.8	-0.67	<1.05	<8.53	0.99
J0238+0124 (31)	221.4	2022 Aug 21	M01,M08	720	0.28	<8.34	7.5	-0.36	<0.84	<8.70	0.92
J0357+1808 (34)	164.4	2022 Aug 24	M01,M08	180	0.63	<8.43	8.3	-0.27	<0.13	<8.70	1.36
J0820+5431 (2)	170.1	2023 Apr 12	M01 ^a	3240	0.19	<7.94	6.6	-0.82	<1.34	<8.76	1.33
J0825+1846 (3)	167.1	2022 Oct 7	M01,M08	540	0.41	<8.26	7.2	-0.30	<1.06	<8.54	1.08
J0827+1059 (39)	192.7	2022 Oct 7	M01,M08	900	0.25	<8.17	7.2	-0.46	<0.97	<8.62	1.17
J0837+1823 (41)	180.8	2022 Oct 8	M01,M08	540	0.33	<8.23	7.3	-0.31	<0.93	<8.54	1.61
J0922+6324 (47)	173.4	2022 Oct 26	M01,M08	1440	0.37	<8.25	6.9	-0.71	<1.35	<8.96	0.98
J0926+4504 (4)	186.7	2022 Oct 8	M01 ^a	900	0.33	<8.26	7.2	-0.64	<1.06	<8.90	1.46
J1026+0426 (54)	186.3	2021 Feb 15	M01 ^a	2160	0.16	7.73 ^b	7.1	-0.66	0.63	8.39	0.79
J1032+4919 (5)	194.8	2022 Oct 8	M01 ^a	360	1.24	<8.87	8.0	-0.05	<0.87	<8.93	1.32
J1035+1400 (57)	175.2	2022 Oct 23	M01,M08	180	0.79	<8.58	7.6	-0.85	<0.98	<9.43	1.10
J1113+0301 (66)	101.8	2022 Oct 23	M01,M08	360	0.49	<7.91	6.8	-0.66	<1.11	<8.57	1.29
J1123+2050 (67)	144.0	2022 Oct 23	M01,M08	180	0.82	<8.43	8.6	0.17	<-0.17	<8.26	0.97
J1132+0809 (68)	219.6	2022 Nov 7	M01,M08	1620	0.17	8.24 ^c	7.2	-0.24	1.04	8.48	1.27
..	9.56 ^d	7.2	-0.24	2.36	9.80	1.27
J1136+3427 (69)	153.5	2022 Nov 4	M01,M08	1620	0.22	<7.91	6.7	-1.31	<1.21	<9.22	..
J1139+0040 (70)	184.0	2022 Nov 17	M01,M08	180	0.80	<8.63	8.0	-0.47	<0.63	<9.11	1.05
J1323-0132 (6)	97.8	2022 Dec 18	M01,M08	180	0.90	<8.13	7.1	-0.43	<1.03	<8.56	..
J1347+0755 (88)	193.3	2022 Dec 13	M01,M08	180	1.05	<8.79	8.5	-0.27	<0.29	<9.06	1.04
J1355+4651 (7)	122.9	2022 Dec 18	M01 ^a	540	0.50	<8.08	6.8	-0.66	<1.28	<8.74	1.18
J1400+1951 (90)	237.2	2023 Apr 12	M01,M08	2880	0.17	<8.18	7.1	-0.63	<1.08	<8.81	1.33
J1444+0409 (9)	170.9	2022 Dec 24	M01,M08	540	0.48	<8.35	7.3	-0.51	<1.05	<8.85	1.20
J1509+3731 (10)	143.0	2022 Aug 24	M01 ^a	180	1.11	<8.56	8.1	0.21	<0.46	<8.35	1.20
J1556+4806 (12)	223.3	2022 Aug 24	M01 ^a	360	0.50	<8.60	7.9	0.03	<0.70	<8.56	0.98
J1602+1445 (106)	159.9	2023 Jan 11	M01,M08	180	1.10	<8.65	8.0	-0.44	<0.65	<9.09	1.22
J1608+3528 (13)	143.6	2023 Jan 4	M01 ^a	180	1.29	<8.62	7.5	-0.35	<1.12	<8.97	1.55
J2320+1225 (122)	185.2	2023 May 18	M01,M08	2700	0.15	<7.91	6.8	-0.69	<1.11	<8.60	1.00

NOTE— Column (1): Source name in increasing R.A. order with the identifiers used by Yang et al. (2017a) in brackets.

Column (2): D_L , luminosity distance in Mpc, estimated using cosmological parameters, $H_0 = 70 \text{ km s}^{-1} \text{ Mpc}^{-1}$, $\Omega_m = 0.3$, $\Omega_\Lambda = 0.7$. Column (3): date of observation. Column (4): beam(s) used in final HI spectra. Column (5): ON target source time per beam in seconds. Column (6): ΔS_{rms} (1σ), noise level per $\sim 10 \text{ km s}^{-1}$ in mJy. Column (7): $\log M_{HI}$, logarithm of the total HI mass in M_\odot . Column (8): $\log M_*$, logarithm of the total stellar mass in M_\odot from Yang et al. (2017a). Column (9): logarithm of star formation rate in $M_\odot \text{ yr}^{-1}$ from Yang et al. (2017a). Column (10): logarithm of HI gas fraction (f_{HI}). Column (11): logarithm of HI gas depletion time scale in years. Column (12): logarithm of $\text{O32} \equiv \text{O}[\text{III}]\lambda 5007 / \text{O}[\text{II}]\lambda 3727$ ratio estimated from the line fluxes in the ViZier Online data catalog (<https://cdsarc.cds.unistra.fr/viz-bin/cat/J/ApJ/847/38>) of Yang et al. (2017a).

^aThe coordinates for beam M08 do not coincide with the source position or ON source coordinates for beam M01. Hence only the spectrum from beam M01 has been used.

^bHI mass of BB J1026+0426 calculated assuming that the ratio of HI mass of BB to HI mass of the neighboring galaxy is equal to their stellar mass ratio. The total HI mass is estimated to be $10^{9.84} M_\odot$ using integrated line flux density of $0.84 \pm 0.05 \text{ Jy km s}^{-1}$. The spectral line for J1026+0426 has HI velocity (V_{HI}) of $12662.3 \pm 2.2 \text{ km s}^{-1}$, FWHM of $148.8 \pm 4.4 \text{ km s}^{-1}$ and peak flux density of $6.9 \pm 0.4 \text{ mJy}$.

^cHI mass of BB J1132+0809 calculated assuming that the ratio of HI mass of BB to HI mass of the neighboring galaxy is equal to their stellar mass ratio. The total HI mass is estimated to be $10^{9.56} M_\odot$ using integrated line flux density of $0.32 \pm 0.03 \text{ Jy km s}^{-1}$. The spectral line for J1132+0809 has HI velocity (V_{HI}) of $14791.1 \pm 3.6 \text{ km s}^{-1}$, FWHM of $124.4 \pm 7.3 \text{ km s}^{-1}$ and peak flux density of $3.0 \pm 0.2 \text{ mJy}$.

^dHI mass of BB J1132+0809 calculated assuming that there is no neighboring galaxy at its redshift. It is equal to the total HI mass $\sim 10^{9.56} M_\odot$ using integrated line flux density of $0.32 \pm 0.03 \text{ Jy km s}^{-1}$.

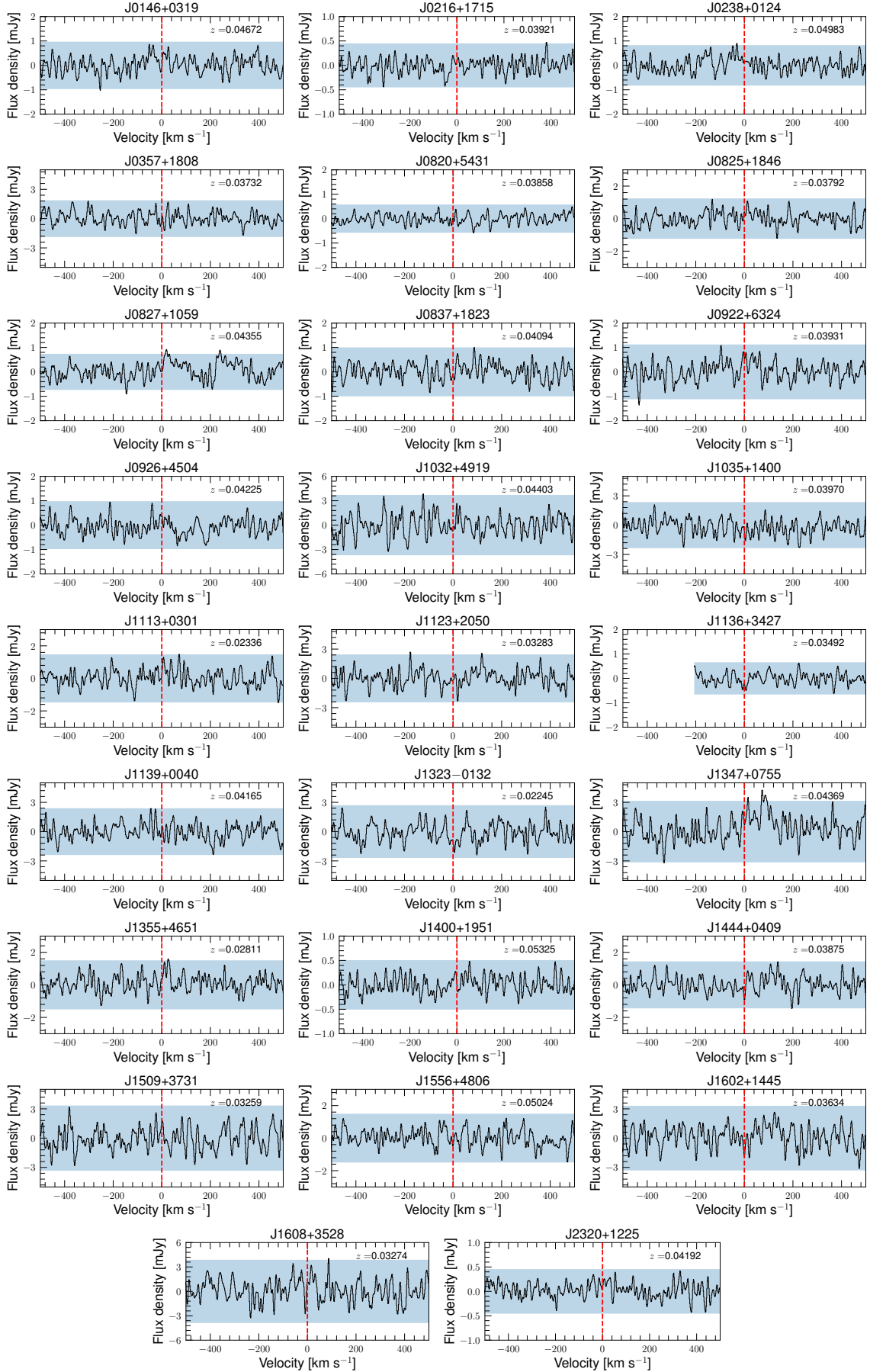


Figure 2. Spectra of blueberry galaxies with HI nondetections. The symbols mean the same as in Fig. 1.

To reduce the data we used a self-developed Python-based pipeline. The pipeline first combines raw data and then separates the data from each ON-OFF cycle for processing. For each ON-OFF cycle, after separating the power values, $P_{\text{on}}^{\text{cal}}$ and $P_{\text{off}}^{\text{cal}}$ with calibration ON and calibration OFF, we use equations

$$T_{\text{a,on}}^{\text{cal}} = P_{\text{on}}^{\text{cal}} T_{\text{cal}} / (P_{\text{on}}^{\text{cal}} - P_{\text{off}}^{\text{cal}}) - T_{\text{cal}}, \quad (1)$$

$$T_{\text{a,off}}^{\text{cal}} = P_{\text{off}}^{\text{cal}} T_{\text{cal}} / (P_{\text{on}}^{\text{cal}} - P_{\text{off}}^{\text{cal}}) \quad (2)$$

to convert power into antenna temperatures, $T_{\text{a,on}}^{\text{cal}}$ and $T_{\text{a,off}}^{\text{cal}}$ for calibration ON and OFF data, respectively. T_{cal} is the temperature of the noise injected for calibration. We then get the average of $T_{\text{a,on}}^{\text{cal}}$ and $T_{\text{a,off}}^{\text{cal}}$ to obtain antenna temperature, T_{a} . We mask antenna temperature for RFI in time and frequency. The antenna temperature values are separated for ON and OFF positions, averaged in time, and then OFF position values are subtracted from ON position values to obtain brightness temperature,

$$T_{\text{b}} = T_{\text{a,ON}} - T_{\text{a,OFF}}, \quad (3)$$

where $T_{\text{a,ON}}$ and $T_{\text{a,OFF}}$ are antenna temperatures at the ON and OFF positions, respectively. The brightness temperature values from all ON-OFF cycles are then averaged together. Thereafter, a sine function and high-degree polynomial are subtracted from two polarizations XX and YY separately to remove baseline ripples and continuum. After that, we average the data from two polarizations and convert K into Jy, using the gain values from Jiang et al. (2020) for zenith angle $< 26.^\circ 4$ and equation (3) of Zhang et al. (2019) for zenith angle $> 26.^\circ 4$. The frequencies are converted to velocities and corrected to a heliocentric frame of rest using the `astropy` library. We averaged the spectra from two different beams M01 and M08 if their ON and OFF positions coincide on target sources. Finally, the spectra were Hanning smoothed to the velocity resolution of $\sim 10 \text{ km s}^{-1}$ from the original resolution of $\sim 7.63 \text{ kHz}$ ($\sim 1.7 \text{ km s}^{-1}$).

3. RESULTS AND DISCUSSION

Of the 28 sources observed with the FAST, we detected HI emission with greater than 5σ significance toward only two galaxies, namely J1026+0426 (BB 54 in Yang et al. (2017a)) and J1132+0809 (BB 68 in Yang et al. (2017a)). The profile toward J1026+0426 resembles a typical profile for a spiral galaxy and the profile toward J1132+0809 is an asymmetric profile. J1026+0426 has a neighboring spiral (Sbc) galaxy SDSS J102640.64+042716.2 of stellar mass¹ $\sim 10^{9.2} M_{\odot}$ at an

angular distance of $\sim 43.''6$ (projected distance $\sim 36.3 \text{ kpc}$) from J1026+0426 and $z \sim 0.04222$ (Ahumada et al. 2020). The $3'$ beam of FAST cannot distinguish the HI associated with J1026+0426 and the spiral galaxy. The optical systemic velocity of spiral galaxy $\sim 12657.2 \text{ km s}^{-1}$ is closer to the HI velocity² (V_{HI}) $\sim 12662.3 \text{ km s}^{-1}$ obtained from the profile suggesting the possibility of HI gas largely being associated with it (see Fig. 1 upper panel). However, the peak flux density in the profile is close to the optical velocity of BB J1026+0426, suggesting that some HI gas is also associated with the BB. For J1132+0809, we searched for neighboring galaxies within a $1.15'$ radius for possible confusing sources. In the SDSS optical image, there is a southern small blue galaxy (hereafter blue galaxy) J113259.13+080930.6 at an angular distance $\sim 12''$ with no spectroscopic redshift but a photometric redshift of 0.004 ± 0.0346 in SDSS DR16 (Ahumada et al. 2020). Since the photometric redshift of the blue galaxy has a large difference with the HI velocity and optical spectroscopic redshift of BB J1132+0809, it suggests that a significant amount of HI at the redshift of ~ 0.04944 is associated with the BB J1132+0809. However, we also checked HI in the FAST spectrum at the photometric redshift within the error range and did not detect any HI. Hence, further optical spectroscopic observations would be required to verify the redshift. If the photometric redshift is incorrect and assuming that the blue galaxy has a redshift corresponding to the HI velocity, we estimate its stellar mass to be $\sim 10^{8.5} M_{\odot}$. We also have a tentative marginal 3σ signal toward J1347+0755 (BB 88) which needs to be confirmed from deeper observations. We consider it as a nondetection for our analysis. The spectrum toward J0827+1059 is partly affected by bandpass ripples and we consider it as a nondetection. J1509+3731 (BB 10) has been observed earlier by Kanekar et al. (2021) and Dutta et al. (2024) where Dutta et al. (2024) has a detection from deeper GMRT observations. In our observations, the noise levels are higher for this source and hence we provide a nondetection spectrum for J1509+3731. For the detections, we provide the HI parameters such as HI velocity (V_{HI}), FWHM, integrated line flux density, and peak flux density in the notes of Table 1. We used the Arecibo IDL routine `mbmeasure` for estimating these parameters. We estimated the errors on these parameters using the method given in Koribalski et al. (2004). We estimate the HI masses using the equation

$$M_{\text{HI}} \sim 2.36 \times 10^5 \times \left(\frac{D_{\text{L}}}{\text{Mpc}} \right)^2 \times \left(\frac{F_{\text{HI}}}{\text{Jy km s}^{-1}} \right) M_{\odot}, \quad (4)$$

¹ Estimated using the same method as Chandola et al. (2024).

² Obtained as the average of velocities corresponding to the FWHM.

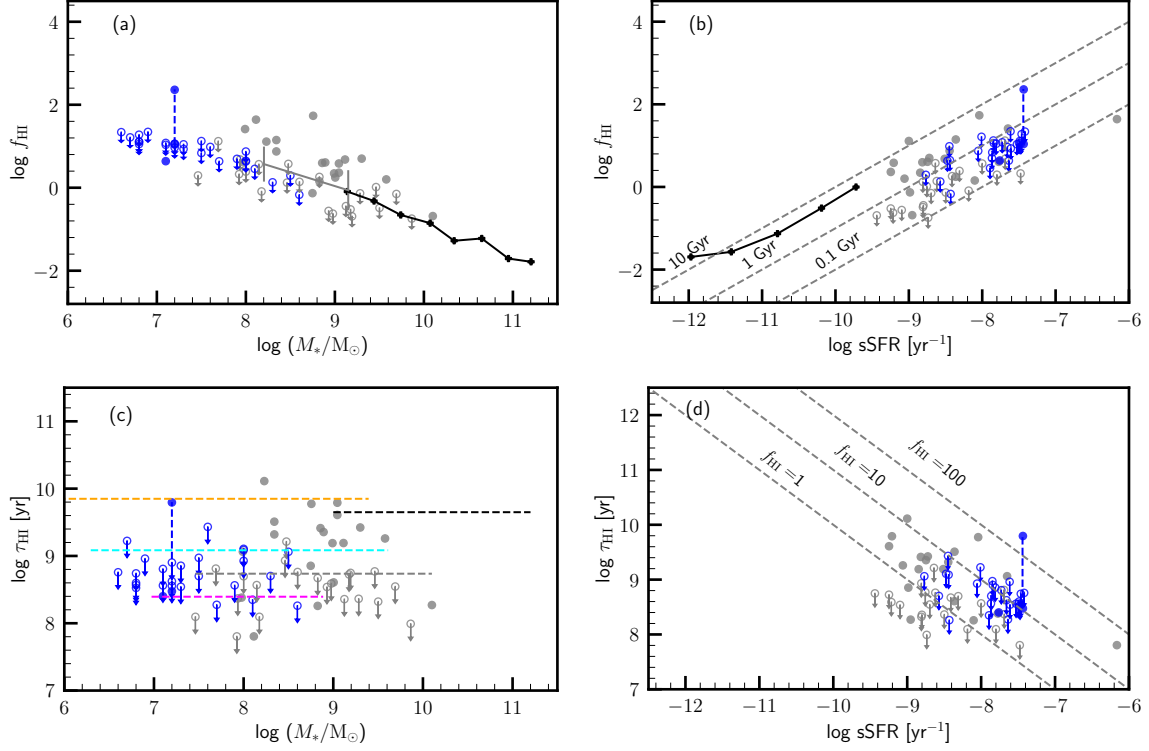


Figure 3. (a): f_{HI} vs. M_* . BBs observed with the FAST are shown with blue-colored circles. Gray-colored circles represent GPs with HI study by Kanekar et al. (2021). Filled and empty circles represent detections and nondetections, respectively. Median values of $\log f_{\text{HI}}$ for respective median $\log M_*$ values for main-sequence galaxies from Catinella et al. (2018) are shown with black connected dots. Similarly, gray connected error bars mark the median $\log f_{\text{HI}}$ values at low and high stellar mass bins for GPs, respectively. The error bars represent the median absolute deviation (MAD) values of $\log f_{\text{HI}}$ at low and high stellar mass bins. For BB J1132+0809, we show the two f_{HI} values, one with the consideration that there is no neighboring galaxy (higher f_{HI}) and the other in the case that the neighboring blue galaxy is at a similar redshift (lower f_{HI}), connected with the dashed blue vertical line. (b): f_{HI} vs. sSFR. Symbols mean the same as in panel (a). Median values of $\log f_{\text{HI}}$ for respective median $\log \text{sSFR}$ values for main-sequence galaxies from Catinella et al. (2018) are shown with black connected dots. Dashed gray diagonal lines mark the HI depletion time scale (τ_{HI}). (c): τ_{HI} vs. M_* . The dashed horizontal black line marks the median τ_{HI} for main-sequence galaxies from Saintonge et al. (2016) and Catinella et al. (2018). Dashed horizontal magenta, cyan, and orange colored lines mark the median τ_{HI} for mid-infrared bright BCDs in the Arcibo sample, all mid-infrared bright BCDs and other non-mid-infrared bright dwarf irregulars or BCDs, respectively, from Chandola et al. (2024). The gray dashed horizontal line marks the median τ_{HI} value for GPs from Kanekar et al. (2021). For BB J1132+0809, we show two values of τ_{HI} , connected with the blue dashed vertical line for the two cases mentioned earlier. (d): τ_{HI} vs. sSFR. Dashed gray diagonal lines mark the HI gas fraction. Other symbols mean the same as in panel (c).

where

$$F_{\text{HI}} = \int \frac{S(v)}{Jy} \frac{dv}{\text{km s}^{-1}} \quad (5)$$

is the integrated line flux density and D_L is the luminosity distance. The estimated HI masses for J1026+0426 and J1132+0809 from the HI profiles, are $6.9 \times 10^9 M_\odot$ and $3.6 \times 10^9 M_\odot$, respectively. We calculate the expected HI mass of J1026+0426 to be $\sim 5.4 \times 10^7 M_\odot$ assuming that the HI mass ratio of the BB and its neighboring galaxy is equal to their stellar mass ratio. Similarly, in the case of J1132+0809, if the photometric redshift of neighboring blue galaxy is incorrect and has a redshift similar to the BB or HI velocity, the expected HI

mass of BB would be $\sim 1.7 \times 10^8 M_\odot$. We have listed the spectral RMS noise (ΔS_{rms}) per channel and HI mass upper limits for all 26 BBs with nondetections in Table 1, and shown their spectra in Figure 2. The RMS noise varies from 0.15 mJy to 1.29 mJy per 10 km s^{-1} . The upper limits on HI masses are estimated using the equation,

$$M_{\text{HI}} \sim 2.36 \times 10^5 \times \left(\frac{D_L}{\text{Mpc}} \right)^2 \times 3 \Delta S_{\text{rms}} \Delta v \sqrt{\frac{50}{\Delta v}} M_\odot, \quad (6)$$

where $\Delta v (= 10 \text{ km s}^{-1})$ is spectral velocity resolution in the spectra and we assume the typical width of the line to be 50 km s^{-1} . The median 3σ upper limit on HI mass is $2.0 \times 10^8 M_\odot$. We also list other properties such

as stellar mass, SFR, HI gas fraction, depletion time scale and O32 ratio obtained from Yang et al. (2017a) in Table 1.

3.1. HI gas fraction (f_{HI})

The atomic hydrogen gas fraction or HI-to-stellar mass ratio ($f_{\text{HI}} = \frac{M_{\text{HI}}}{M_*}$) has been used as a measure of fuel reservoir available per unit stellar mass and baryonic composition of galaxies in the literature. It strongly depends on the stellar mass and star-forming nature of the galaxies (Chandola et al. 2024). The galaxies with lower stellar mass are found to have higher HI gas fraction implying atomic hydrogen is the dominant baryonic component (Saintonge et al. 2016; Thuan et al. 2016; Catinella et al. 2018; Kanekar et al. 2021; Chandola et al. 2024). HI gas fraction for main-sequence galaxies ($>10^9 M_{\odot}$) at nearby redshifts are found to be quite low, reaching up to ~ 0.02 at the highest stellar mass ($\sim 10^{11} M_{\odot}$) to ~ 1 at $\sim 10^9 M_{\odot}$ (see black dots connected with black line in Figure 3 (a)) in the extended Galaxy Evolution Explorer (GALEX) Arecibo SDSS Survey (xGASS; Catinella et al. 2018). For the sample of GPs at the redshift <0.1 , Kanekar et al. (2021) found that gas fraction further increases at lower stellar mass Green Peas, consistent with the scenario of the dominance of atomic hydrogen in baryonic composition. For the BCDs of lower stellar masses ($\lesssim 10^8 M_{\odot}$), the typical HI gas fractions are found to be higher (~ 10) but with a lot of dispersion (Chandola et al. 2024; Thuan et al. 2016).

We have plotted f_{HI} vs stellar mass and specific star formation rate (sSFR) in panels (a) and (b), respectively, of Figure 3. In our study of BBs which have lower stellar masses than GPs, we made observations such that the galaxies following $f_{\text{HI}}-M_*$ relation at lower stellar masses are detected with at least 3σ significance. Hence, we found that the f_{HI} upper limits for BBs are similar to the upper limits for GPs for a similar common stellar mass range. The median 3σ upper limit on f_{HI} for BBs is 10.2. It is lower than the expected value of ~ 14.6 at the median stellar mass of $10^{7.3} M_{\odot}$ from extrapolating $f_{\text{HI}}-M_*$ relation for GPs and main-sequence galaxies. Also, the majority of GPs and BBs due to their starburst nature appear to deviate from the $f_{\text{HI}}-\text{sSFR}$ relation for the main-sequence star-forming galaxies and have lower f_{HI} than expected. Considering the neighboring galaxy, we expect f_{HI} of 4.3 for J1026+0426. For J1123+0809, if there is no neighboring galaxy, we estimate f_{HI} to be ~ 229 . However, if the neighboring blue galaxy has a redshift corresponding to the HI velocity, we expect a gas fraction of ~ 11.0 for J1132+0809. We show both values of f_{HI} for J1132+0809 connected with vertical dashed lines in the upper panels of Figure 3.

3.2. HI depletion time scale (τ_{HI})

HI depletion time scale ($\tau_{\text{HI}} = \frac{M_{\text{HI}}}{\text{SFR}}$) is a measure of how fast and efficiently the atomic gas reservoir is being used. In Figure 3 (lower panels), we have shown HI depletion time scale vs stellar mass and sSFR. The expected HI depletion time scale for J1026+0426 is 0.25 Gyr. For J1132+0809, the depletion time scale can be ~ 6.3 Gyr if there is no neighboring galaxy, and ~ 0.3 Gyr if the neighboring blue galaxy has a redshift corresponding to the HI velocity. The median 3σ upper limit on the depletion time scale from nondetections is 0.53 Gyr. This median upper limit on the HI depletion timescale is similar to the depletion time scale of low redshift GPs by Kanekar et al. (2021) and slightly higher than mid-IR bright BCDs in the Arecibo sample by Chandola et al. (2024). However, this is about 1 order of magnitude lower than τ_{HI} for the local main sequence galaxies (Saintonge et al. 2016; Catinella et al. 2018) or other non-mid-IR bright dwarf irregulars or BCDs in the literature (Chandola et al. 2024). This implies that the BBs have depleted their atomic gas reservoir or are in the process of depleting it quite fast. When the atomic gas depletion time scales (~ 5 Gyr) are larger than the molecular gas depletion time scales (~ 1 Gyr), as in the case of local main sequence galaxies, it has less effect on the star formation, as sufficient atomic gas is available for conversion to molecular gas (Saintonge et al. 2016; Catinella et al. 2018). However, for starburst systems like BBs and GPs, shorter atomic gas depletion timescales are critical as the atomic gas might get converted faster into molecular gas due to favorable conditions like high density, and soon there could be a scarcity of atomic gas if not replenished from the nearby environment (Chandola et al. 2024). It would require further observations of molecular gas toward these sources as the HI to H_2 scaling relation for main-sequence galaxies may not be applicable in the case of extreme starburst, low metallicity BBs or GPs.

3.3. HI properties, O32 ratio, and Lyman Escape fraction

The HI detection rate³ in BBs ($7.1_{-4.6}^{+9.4}$ %) is significantly lower compared to the previous detection rate of $\sim 48\%$ for GPs by Kanekar et al. (2021) when observed at similar levels of HI mass and depletion time scale (or star-formation efficiency) upper limits. This detection rate is also low compared to low metallicity BCDs of similar stellar masses reported earlier in the literature (e.g. Thuan et al. 2016). Kanekar et al. (2021) reported

³ The 1σ error on detection rate is estimated using Gehrels (1986) small number statistics for Poisson distribution.

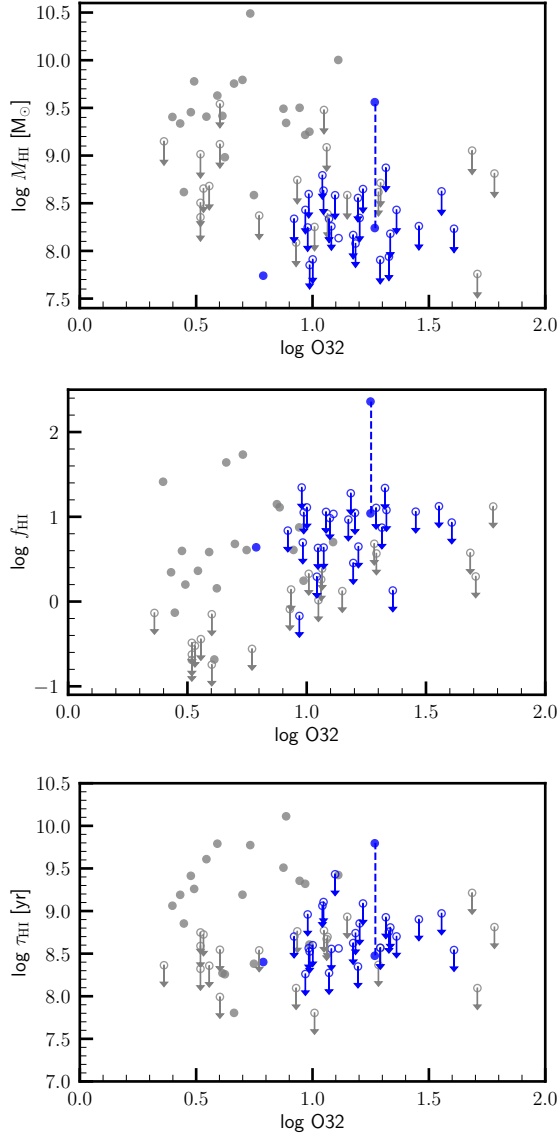


Figure 4. Top panel: M_{HI} vs. $\text{O32} \equiv \text{O}[\text{III}]\lambda 5007/\text{O}[\text{II}]\lambda 3727$ ratio. Middle panel: f_{HI} vs. $\text{O32} \equiv \text{O}[\text{III}]\lambda 5007/\text{O}[\text{II}]\lambda 3727$ ratio. Bottom panel: τ_{HI} vs. $\text{O32} \equiv \text{O}[\text{III}]\lambda 5007/\text{O}[\text{II}]\lambda 3727$ ratio. The symbols mean the same as in Fig. 3.

that GPs with an O32 ratio higher than 10 have lower detection rate ($\sim 9\%$) than those with lower O32 values ($\sim 62\%$). Of the 28 sources observed, we have O[II] $\lambda 3727$ flux values available for only 26 sources from Yang et al. (2017a). We find that all 26 BBs have an O32 ratio greater than 8.3, and the majority (20/26) of the BBs have O32 values $\gtrsim 10$. Hence, our finding of a low detection rate for BBs is similar to that for GPs of O32 $\gtrsim 10$ by Kanekar et al. (2021). Of the two detections, J1026+0426 has an O32 value ~ 6.2 , while J1132+0809 has an O32 value ~ 18.6 , only the third HI detection of BBs or GPs with an O32 ratio $\gtrsim 10$ in the literature,

the previous two being J1200+2719 by Kanekar et al. (2021) and J1509+3731 by Dutta et al. (2024).

We have also plotted M_{HI} , f_{HI} and τ_{HI} vs O32 in the upper, middle, and lower panels of Figure 4, respectively. The median 3σ upper limit on M_{HI} for BBs with higher O32 is lower than M_{HI} values for GPs with lower O32. This is expected, as O32 tends to have higher values for lower stellar mass (Nakajima & Ouchi 2014; Paalvast et al. 2018; Shen et al. 2024), and high O32 selection for BBs gives lower stellar masses (Yang et al. 2017a; Izotov et al. 2016). Hence, the lower M_{HI} values or upper limits for BBs are according to the $M_{\text{HI}}-M_*$ relation (e.g. Huang et al. 2012). We further plot M_{HI} normalized with M_* i.e. gas fraction (f_{HI}) vs O32. In this plot, the upper limits on f_{HI} appear to increase with increasing O32 or decreasing stellar mass. Hence, the low HI detection rates at higher O32 could be the effect of both f_{HI} sensitivity and ionization parameter indicator O32 (Kewley & Dopita 2002; Nakajima & Ouchi 2014; Shen et al. 2024). In the common O32 range, the f_{HI} upper limits for BBs are slightly higher than GPs, suggesting the need for deeper observations and indicating f_{HI} lower than expected from $f_{\text{HI}}-M_*$ as shown in Figure 3 panel (a). In the τ_{HI} vs O32 plot, we find the median 3σ upper limit on τ_{HI} for BBs is lower than τ_{HI} values for GPs of lower O32.

The O32 ratio has been discussed in some previous studies as an indirect indicator of the Lyman escape fraction or leakage (Jaskot & Oey 2013; Izotov et al. 2016, 2018a,b). However, O32 has a weak correlation with Lyman escape fraction (Izotov et al. 2018b, 2021) and there have been suggestions to combine O32 ratios with other proxies such as SFR surface density, Ly α line widths, and Ly α peak velocity separation (Izotov et al. 2021; Flury et al. 2022; Yang et al. 2017b) to search for LyC leakers. Nevertheless, a high O32 ratio is one of the conditions fulfilled by BBs for a possible high Lyman escape fraction, making them the high potential candidates. The chances of LyC or Ly α photons escaping from a galaxy or getting absorbed also depend upon the distribution of neutral hydrogen gas in the interstellar medium (ISM). The porous nature, or low column density (Henry et al. 2015), or low covering fraction (McKinney et al. 2019) in the distribution of HI gas in the ISM can allow LyC or Ly α photons to escape. Recently, in the HI study of the nearest LyC emitting source, Haro 11, Le Reste et al. (2024) found HI distribution with offset from the LyC production site due to mergers and facilitating the escape of Ly α or LyC photons. The interferometric HI studies of GP J0213+0056 by Purkayastha et al. (2022) and BB J1509+3731 by Dutta et al. (2024) also suggest a similar scenario of dis-

turbed HI morphology with offset from the peak starburst region due to mergers or interaction. To explore this in detail for our detections, we need interferometric observations of the HI gas distribution, and also an accurate determination of the redshift of the neighboring galaxy of BB 1132+0809.

4. SUMMARY

From our study of 28 BBs with FAST, we report the HI detection toward two BBs, J1026+0426 and J1132+0809. For BB J1026+0426 we estimate its HI mass to be $\sim 5.4 \times 10^7 M_{\odot}$ considering HI contribution from its neighboring galaxy to the total HI mass of $\sim 6.9 \times 10^9 M_{\odot}$. For BB J1132+0809 the photometric redshift of the neighboring galaxy is significantly different. The HI mass has been estimated to be $\sim 3.6 \times 10^9 M_{\odot}$. However, if the neighboring galaxy has a redshift similar to the BB, the HI mass is estimated to be $\sim 1.7 \times 10^8 M_{\odot}$. From the nondetections, we have a median 3σ upper limit of $2.0 \times 10^8 M_{\odot}$ on HI mass. HI gas fractions for BBs tend to have lower values than expected from $f_{\text{HI}}\text{-SFR}$ or $f_{\text{HI}}\text{-}M_{*}$ relations for local main-sequence galaxies. These galaxies have a median 3σ upper limit on HI depletion time scale ~ 0.5 Gyr, nearly 1 order of magnitude lower compared to τ_{HI} for local main-sequence galaxies. The HI detection rate for these galaxies is also significantly low ($\sim 7\%$) as compared to higher stellar mass GPs by Kanekar et al. (2021) but similar to GPs with high $\text{O}32 \equiv \text{O}[\text{III}]\lambda 5007 / \text{O}[\text{II}]\lambda 3727$ ratios in their sample.

ACKNOWLEDGMENTS

We thank the anonymous reviewer for the constructive and helpful comments that helped to significantly improve the manuscript. Y.C. thanks the Center for Astronomical Mega-Science, Chinese Academy of Sciences, for the FAST distinguished young researcher fellowship (19-FAST-02). Y.C. also acknowledges the support from the National Natural Science Foundation of China (NSFC) under grant No. 12050410259 and the Ministry of Science and Technology (MOST) of China grant no. QNJ2021061003L. C.W.T. is supported by NSFC grant Nos. 11988101 and 12041302. Y.Z.M. acknowledges the support from the National Research Foundation of South Africa with grant Nos. 150580, 159044, CHN22111069370 and ERC23040389081. Y.C. thanks IUCAA for its hospitality while finishing this work. This work has used the data from the Five-hundred-meter Aperture Spherical radio Telescope (FAST). FAST is a Chinese national mega-science facility, operated by the National Astronomical Observatories of the Chinese Academy of Sciences (NAOC).

Facility: FAST:500m.

Software: Python, Numpy (Harris et al. 2020), Matplotlib (Hunter 2007), Astropy (Astropy Collaboration et al. 2013, 2018, 2022), TOPCAT (Taylor 2005)

REFERENCES

- Abazajian, K. N., Adelman-McCarthy, J. K., Agüeros, M. A., et al. 2009, *ApJS*, 182, 543, doi: [10.1088/0067-0049/182/2/543](https://doi.org/10.1088/0067-0049/182/2/543)
- Ahumada, R., Allende Prieto, C., Almeida, A., et al. 2020, *ApJS*, 249, 3, doi: [10.3847/1538-4365/ab929e](https://doi.org/10.3847/1538-4365/ab929e)
- Astropy Collaboration, Robitaille, T. P., Tollerud, E. J., et al. 2013, *A&A*, 558, A33, doi: [10.1051/0004-6361/201322068](https://doi.org/10.1051/0004-6361/201322068)
- Astropy Collaboration, Price-Whelan, A. M., Sipőcz, B. M., et al. 2018, *AJ*, 156, 123, doi: [10.3847/1538-3881/aabc4f](https://doi.org/10.3847/1538-3881/aabc4f)
- Astropy Collaboration, Price-Whelan, A. M., Lim, P. L., et al. 2022, *ApJ*, 935, 167, doi: [10.3847/1538-4357/ac7c74](https://doi.org/10.3847/1538-4357/ac7c74)
- Baldwin, J. A., Phillips, M. M., & Terlevich, R. 1981, *PASP*, 93, 5, doi: [10.1086/130766](https://doi.org/10.1086/130766)
- Cardamone, C., Schawinski, K., Sarzi, M., et al. 2009, *MNRAS*, 399, 1191, doi: [10.1111/j.1365-2966.2009.15383.x](https://doi.org/10.1111/j.1365-2966.2009.15383.x)
- Catinella, B., Saintonge, A., Janowiecki, S., et al. 2018, *MNRAS*, 476, 875, doi: [10.1093/mnras/sty089](https://doi.org/10.1093/mnras/sty089)
- Chandola, Y., Li, D., Tsai, C.-W., et al. 2024, *MNRAS*, 527, 603, doi: [10.1093/mnras/stad3018](https://doi.org/10.1093/mnras/stad3018)
- Dutta, S., Bera, A., Bait, O., et al. 2024, *MNRAS*, 531, 5140, doi: [10.1093/mnras/stae1490](https://doi.org/10.1093/mnras/stae1490)
- Flury, S. R., Jaskot, A. E., Ferguson, H. C., et al. 2022, *ApJ*, 930, 126, doi: [10.3847/1538-4357/ac61e4](https://doi.org/10.3847/1538-4357/ac61e4)
- Gawiser, E., Francke, H., Lai, K., et al. 2007, *ApJ*, 671, 278, doi: [10.1086/522955](https://doi.org/10.1086/522955)
- Gehrels, N. 1986, *ApJ*, 303, 336, doi: [10.1086/164079](https://doi.org/10.1086/164079)
- Gil de Paz, A., Madore, B. F., & Pevunova, O. 2003, *ApJS*, 147, 29, doi: [10.1086/374737](https://doi.org/10.1086/374737)
- Harris, C. R., Millman, K. J., van der Walt, S. J., et al. 2020, *Nature*, 585, 357, doi: [10.1038/s41586-020-2649-2](https://doi.org/10.1038/s41586-020-2649-2)
- Henry, A., Scarlata, C., Martin, C. L., & Erb, D. 2015, *ApJ*, 809, 19, doi: [10.1088/0004-637X/809/1/19](https://doi.org/10.1088/0004-637X/809/1/19)

- Huang, S., Haynes, M. P., Giovanelli, R., & Brinchmann, J. 2012, *ApJ*, 756, 113, doi: [10.1088/0004-637X/756/2/113](https://doi.org/10.1088/0004-637X/756/2/113)
- Hunter, J. D. 2007, *Computing in Science & Engineering*, 9, 90, doi: [10.1109/MCSE.2007.55](https://doi.org/10.1109/MCSE.2007.55)
- Izotov, Y. I., Schaerer, D., Thuan, T. X., et al. 2016, *MNRAS*, 461, 3683, doi: [10.1093/mnras/stw1205](https://doi.org/10.1093/mnras/stw1205)
- Izotov, Y. I., Schaerer, D., Worseck, G., et al. 2018a, *MNRAS*, 474, 4514, doi: [10.1093/mnras/stx3115](https://doi.org/10.1093/mnras/stx3115)
- Izotov, Y. I., Worseck, G., Schaerer, D., et al. 2021, *MNRAS*, 503, 1734, doi: [10.1093/mnras/stab612](https://doi.org/10.1093/mnras/stab612)
- . 2018b, *MNRAS*, 478, 4851, doi: [10.1093/mnras/sty1378](https://doi.org/10.1093/mnras/sty1378)
- Jaskot, A. E., & Oey, M. S. 2013, *ApJ*, 766, 91, doi: [10.1088/0004-637X/766/2/91](https://doi.org/10.1088/0004-637X/766/2/91)
- Jiang, P., Tang, N.-Y., Hou, L.-G., et al. 2020, *Research in Astronomy and Astrophysics*, 20, 064, doi: [10.1088/1674-4527/20/5/64](https://doi.org/10.1088/1674-4527/20/5/64)
- Jiang, T., Malhotra, S., Rhoads, J. E., & Yang, H. 2019, *ApJ*, 872, 145, doi: [10.3847/1538-4357/aeee8a](https://doi.org/10.3847/1538-4357/aeee8a)
- Kanekar, N., Ghosh, T., Rhoads, J., et al. 2021, *ApJL*, 913, L15, doi: [10.3847/2041-8213/abfb76](https://doi.org/10.3847/2041-8213/abfb76)
- Kewley, L. J., & Dopita, M. A. 2002, *ApJS*, 142, 35, doi: [10.1086/341326](https://doi.org/10.1086/341326)
- Koribalski, B. S., Staveley-Smith, L., Kilborn, V. A., et al. 2004, *AJ*, 128, 16, doi: [10.1086/421744](https://doi.org/10.1086/421744)
- Le Reste, A., Cannon, J. M., Hayes, M. J., et al. 2024, *MNRAS*, 528, 757, doi: [10.1093/mnras/stad3910](https://doi.org/10.1093/mnras/stad3910)
- McKinney, J. H., Jaskot, A. E., Oey, M. S., et al. 2019, *ApJ*, 874, 52, doi: [10.3847/1538-4357/ab08eb](https://doi.org/10.3847/1538-4357/ab08eb)
- Nakajima, K., & Ouchi, M. 2014, *MNRAS*, 442, 900, doi: [10.1093/mnras/stu902](https://doi.org/10.1093/mnras/stu902)
- Nan, R., Li, D., Jin, C., et al. 2011, *International Journal of Modern Physics D*, 20, 989, doi: [10.1142/S0218271811019335](https://doi.org/10.1142/S0218271811019335)
- Paalvast, M., Verhamme, A., Straka, L. A., et al. 2018, *A&A*, 618, A40, doi: [10.1051/0004-6361/201832866](https://doi.org/10.1051/0004-6361/201832866)
- Purkayastha, S., Kanekar, N., Chengalur, J. N., et al. 2022, *ApJL*, 933, L11, doi: [10.3847/2041-8213/ac7522](https://doi.org/10.3847/2041-8213/ac7522)
- Saintonge, A., Catinella, B., Cortese, L., et al. 2016, *MNRAS*, 462, 1749, doi: [10.1093/mnras/stw1715](https://doi.org/10.1093/mnras/stw1715)
- Shen, L., Papovich, C., Matharu, J., et al. 2024, *arXiv e-prints*, arXiv:2410.23349, doi: [10.48550/arXiv.2410.23349](https://doi.org/10.48550/arXiv.2410.23349)
- Taylor, M. B. 2005, in *Astronomical Society of the Pacific Conference Series*, Vol. 347, *Astronomical Data Analysis Software and Systems XIV*, ed. P. Shopbell, M. Britton, & R. Ebert, 29
- Thuan, T. X., Goehring, K. M., Hibbard, J. E., Izotov, Y. I., & Hunt, L. K. 2016, *MNRAS*, 463, 4268, doi: [10.1093/mnras/stw2259](https://doi.org/10.1093/mnras/stw2259)
- Yang, H., Malhotra, S., Rhoads, J. E., & Wang, J. 2017a, *ApJ*, 847, 38, doi: [10.3847/1538-4357/aa8809](https://doi.org/10.3847/1538-4357/aa8809)
- Yang, H., Malhotra, S., Gronke, M., et al. 2017b, *ApJ*, 844, 171, doi: [10.3847/1538-4357/aa7d4d](https://doi.org/10.3847/1538-4357/aa7d4d)
- Zhang, K., Wu, J., Li, D., et al. 2019, *Science China Physics, Mechanics, and Astronomy*, 62, 959506, doi: [10.1007/s11433-019-9383-y](https://doi.org/10.1007/s11433-019-9383-y)